Nano Energy 33 (2017) 410–417

Contents lists available at ScienceDirect

Nano Energy

journal homepage: www.elsevier.com/locate/nanoen

Full paper

Enhancing H_2 evolution by optimizing H adatom combination and desorption over Pd nanocatalyst

Jin Wang, Hongyi Tan, Dan Jiang, Kebin Zhou*

School of Chemistry and Chemical Engineering, University of Chinese Academy of Sciences, Beijing 100049, PR China

ARTICLE INFO

Keywords:
H_2 evolution
Pd catalyst
Formate dehydrogenation
Hydride decomposition

ABSTRACT

Catalytic hydrogen evolution plays a significant role in hydrogen production and utilization. The combinative desorption of hydrogen (Tafel step, i.e., $2H^* \rightarrow H_2$) from metal catalysts has been extensively reported as the rate-determining step. However, a full atomic-level understanding on how the H-Metal binding strength affects on the elementary Tafel steps is still lacking. In the current study, H_2 evolution over Pd catalysts was investigated by combining theoretical and experimental techniques. Density functional theory calculations revealed that H_2 evolution was governed by either the combination barriers of $2H^*$ or the desorption barriers of molecular H_2 from the surface of the palladium catalyst, which was strongly dependent on the size of Pd particles: the rate-limiting step of H_2 evolution for large nanoparticles (NPs) is diffusive combination of H^* across the metal surface, while both $2H^*$ combination and H2 desorption are difficult for subnanometer-sized Pd clusters. By tuning the combined effect of H adatom combination and H_2 desorption, a highly performance Pd catalyst for hydrogen evolution both for temperature-programmed palladium hydride decomposition and catalytic dehydrogenation of formate was designed and synthesized. TiO_2-supported Pd NPs that were 2 nm in size exhibited excellent activity for formate dehydrogenation with an TOF value that was as high as 2184 h^{-1} at 298 K.

1. Introduction

Hydrogen (H_2) is an ideal clean-burning energy carrier and a promising candidate to replace traditional fuels in the near future [1]. Catalytic H_2 production under mild conditions (i.e., electrolysis of water and dehydrogenation of chemical hydrides) has become an attractive topic [2–5]. Due to their unique catalytic performance, Pt-group heterogeneous nanocatalysts have been widely used for hydrogen evolution [6–8]. In general, the overall catalytic reaction involves reactant adsorption, chemical reaction with the formation of adsorbed H atoms, and combinative desorption of molecular H_2. The last step (i.e., $2H^* \rightarrow H_2$) is referred to as the famous Tafel reaction. It has been extensively reported as the rate-determining step in many cases, such as electrocatalytic hydrogen evolution reaction (HER) over Pt/C catalysts [9,10], photocatalytic water splitting on small Ru nanoparticles (NPs) as the cocatalyst [11], as well as hydrogen evolution through catalytic dehydrogenation of formic acid/formate on Pd catalysts [12], This circumstance is even more exaggerated when the catalysts work at room temperature [13–15].

To facilitate hydrogen evolution, numerous studies have been focused on modification of the hydrogen binding energy (HEB) because desorption of H_2 is primarily governed by the binding strength of hydrogen with the metal catalyst [16–18]. Many factors are responsible for HEB, such as the nature of the metals [19,20], local composition [21] and strain in metal particles [17,22]. For example, the adsorption energy of H on one metal could be altered dramatically when bimetallic structure was constructed, due to the changes of strain or heterometallic bonding interactions [17,20,22]. From a microscopic point of view, various types of H atom adsorption sites are present on a metal surface, resulting in *n*-fold adsorption patterns with different bond strengths (*n*=1, 2 or 3, the number of metal atoms that is bonded with H) [23]. The Tafel reaction may involve several reaction steps [24,25] including diffusion of the H adatom across surface metal atoms with various coordinations, combination of two adjacent H adatoms and desorption of molecular hydrogen. Both hydrogen diffusion and H-H recombination would be sensitive to the surface structure of the metal catalyst [25,26]. Therefore, a detailed atomic-level understanding on how the H-M binding strength affects on the elementary Tafel steps would be very useful for the rational development of high-performance hydrogen evolution catalysts.

Herein, density functional theory (DFT) calculations were firstly carried out to investigate the elementary Tafel steps over palladium

* Corresponding author.
E-mail address: kbzhou@ucas.ac.cn (K. Zhou).

http://dx.doi.org/10.1016/j.nanoen.2017.02.001
Received 5 August 2016; Received in revised form 19 January 2017; Accepted 3 February 2017
Available online 06 February 2017

nanocatalyst. It was found that H_2 evolution was governed by either the combination barriers of $2H^*$ or the desorption barriers of molecular H_2 from the surface of the palladium catalyst, which was strongly dependent on the size of Pd particles. Based on this microscopic insight, highly active Pd nanocatalysts for hydrogen evolution (i.e., temperature-programmed palladium hydride decomposition and catalytic dehydrogenation of formate) was designed and synthesized by optimizing these two surface processes through tuning the size of the Pd NPs. TiO_2-supported Pd NPs that were 2 nm in size exhibited excellent activity for formate dehydrogenation with an TOF value that was as high as 2184 h^{-1} at 298 K.

2. Material and methods

2.1. Theoretical calculations

All calculations were performed based on the spin-polarized plane-wave DFT approach with the Vienna ab initio simulation package (VASP). The electron exchange and correlation energies were calculated with the GGA-PW91 functional. The ionic cores and electron-ion interactions were described by the projector augmented wave (PAW) method. The energy cut-off of 500 eV was employed. All geometries were optimized until the difference in total energy smaller than 10^{-4} eV and self-consistent forces on all atoms were less than 0.02 eV $Å^{-1}$. The interaction between H-species with the Pd_n (n=4, 13, 55) clusters was studied using periodic models. These systems were placed into supercells with 20 Å to avoid interaction. The 3×3 supercell surface model of Pd (111) with 4 atomic layers was employed with a vacuum region of 15 Å. Monkhorst-Pack k-point mesh of 3×3×3 was used for Pd_4 and Pd_{13}, single k-point (gamma point) was used for Pd_{55} and Pd (111) surface model. The transition states were optimized by using the climbing-image nudged elastic band method (CI-NEB) at a reduced force threshold of 0.05 eV $Å^{-1}$.

The binding energy per atom E_b and the adsorption energy of H E_{ad} were defined:

$$E_b = -(E_{cluster} - nE_{atom})/n$$

$$E_{ad} = -(E_{H-cluster} - E_H - E_{cluster})$$

where $E_{cluster}$, E_{atom} and E_H are the energies of Pd_n cluster, single Pd atom and single H atom, respectively. $E_{H\text{-}cluster}$ is the total energy of H adsorbed on Pd_n cluster. Here, n is the number of atoms in the Pd clusters.

2.2. Catalysts preparation

All materials used in this study were analytical purity.

2.2.1. Preparation of TiO_2 nanorod

TiO_2 nanorod was also synthesized by using a facile hydrothermal method. 10 mL tetrabutyl titanate ($C_{16}H_{36}O_4Ti$) was added to the mixture solution contain 3 mL H_2O_2 and 3 mL HCl rapidly at room temperature. Then the mixture was transferred to a 50 mL Teflon-lined autoclave and heated at 200 °C for 24 h. After reaction, the products were washed with aqueous NaOH solution (0.2 M, 200 mL), then washed with deionized water and alcohol several times. The white TiO_2 nanorod was dried at 50 °C for 5 h.

2.2.2. Preparation of TiO_2 supported palladium cluster catalyst (0.8 nm-Pd)

0.5 g TiO_2 and 22.4 mg $Pd(OAc)_2$ powders were dispersed in 20 mL anhydrous methanol and sonicated for 1 min, respectively. The solutions were stirred at 298 K for 20 min with exposure to ambient light. Then the two solutions were mixed for just 1 min for depositing of the Pd clusters and avoiding growth of clusters. Subsequently, the solvent and unreduced precursor were removed by centrifuging followed by washing with anhydrous methanol twice and then dried under 30 °C for 2 h.

2.2.3. Preparation of TiO_2 supported 2 nm-palladium nanoparticles catalyst (2 nm-Pd)

0.5 g TiO_2 powders were dispersed in 300 mL deionized water and sonicated for 10 min. An aqueous Na_2PdCl_4 solution (47 mM, 2 mL) was added to the obtained TiO_2 slurry and continuous stirring for 30 min. Then 2 mL sodium citrate ($Na_3C_6H_5O_7$, 0.034 M) aqueous solution was added to the mixture followed by injection of an aqueous $NaBH_4$ solution (0.33 M, 2 mL) under vigorous stirring. The color of mixture changed from canary yellow to brown. After 2 h, the obtained precipitates were washed with deionized water and ethanol and dried at 50 °C for 5 h. The catalysts were denoted as 2 nm-Pd.

2.2.4. Preparation of TiO_2 supported 5 nm-palladium nanoparticles catalyst (5 nm-Pd)

2 mL aqueous Na_2PdCl_4 solution (47 mM) was added to PVA solution (0.02 g, 48 mL). Then the pretreated mixture was put into hot ethanol (50 mL) in a 250 mL round-bottom flask equipped with magnetic stir bar. After refluxing 30 min, the color of the mixture changed from canary yellow to brown, indicating the Pd sol was obtained. Next, the suspension of 0.5 g TiO_2 powders was added to the above Pd sol rapidly with continuous stirring for 2 h. Subsequently, the obtained precipitate was washed with deionized water and ethanol and then dried at 50 °C for 5 h.

2.2.5. Preparation of TiO_2 supported 10 nm-palladium nanoparticles catalyst (10 nm-Pd)

The 10 nm-Pd catalyst was prepared following the colloidal deposition method for 5 nm-Pd (vide supra). The only variation was that sodium citrate solution (0.01 g, 48 mL) is the capping agent instead of PVA.

2.2.6. Preparation of TiO_2 supported 14 nm-palladium nanoparticles catalyst (14 nm-Pd)

The 14 nm-Pd catalyst was prepared following the colloidal deposition method for 5 nm-Pd (vide supra). The only variation was that sodium citrate solution (0.01 g, 48 mL) as the capping agent and cold ethanol as the mild reductant.

All the above obtained catalysts were treated with mixture gases containing 1.0 vol% CO in air at 300 °C for 1 h to remove any impurities, followed by reduced under H_2/Ar gas at 150 °C for 1 h.

2.3. Catalyst characterizations

All of the size and morphology images were obtained with Hitachi H-7650 transmission electron microscope (TEM) and a FEI Tecnai F20 high-resolution transmission electron microscope (HRTEM). HAADF-STEM images were acquired with a JEM-ARM200F at 200 kV. The Pd loading was measured with Varian Vista MPX Inductively Coupled Plasma Optical Emission Spectrometer (ICP-OES). The X-ray diffraction (XRD) measurements for structure and composition determination were carried out with a Bruker D8 Advance X-ray diffractometer with Cu Kα radiation (λ=1.5418 Å), and the data were recorded at a scan rate of 4 degree·min^{-1}. Pd_{3d} photoelectron spectra were taken using X-ray photoelectron spectroscopy (XPS, ESCALAB 250 Xi)with Al Kα radiation.

2.4. Catalyst activity evaluation

Temperature-programmed hydride decomposition (TPHD) analysis was carried out with a ChemiSorb 2720 apparatus equipped with a TCD detector. Prior the experiment, all the catalysts (50 mg) were reduced

with 5 vol% H_2/Ar mixture in a temperature ramp of 10° min^{-1}, up to 150 °C. Then, the catalyst was kept in constant temperature for 20 min and cools them to an ambient temperature. TPD was performed using H_2/Ar mixture as a carrier gas, ramping the temperature from 20 °C to 200 °C. The volumes of gas generated were monitored using RTK-GMA-I Gas Metering Cell.

The catalytic activities for dehydrogenation of aqueous ammonium formate were evaluated at atmospheric pressure and the give temperature was achieved by water bath. In a typical procedure, the catalyst powder (contain 8.4 μmol Pd) dispersed in 5 mL deionized water and sonicated for 10 min, then placed in a reaction vessel (25 mL), which was connected to a automatic Gas Metering Cell. The catalytic reaction was begun once the formate solution (4 M, 5 mL) was added into the reactor with magnetic stirring (300 r/min). The composition of gas generated was measured by using a gas chromatograph analysis system (GC) equipped with a TCD detector. The trace CO_2 and CO concentrations in the H_2-containing stream were measured by using a GC equipped with a FID detector. Initial turnover frequencies (TOFs) were measured within the first 10 min, where the dispersions of metal atoms were calculated from the CO chemisorptions.

3. Results and discussion

It is well known that palladium hydride (PdH_x) can be easily formed once palladium contacts hydrogen even at room temperature [27]. Therefore, both of pure Pd structures and their hydride counterparts have been constructed.

The optimized pure Pd structures are shown in Figs. 1 and S1. The binding energies (E_b) of clusters are 1.63, 2.32 and 2.90 eV for Pd_4, Pd_{13} and Pd_{55}, respectively [28,29]. Pd (111) surface was chosen to represent large Pd NPs because it is the most stable surface of close-packed Pd metal. Pd (111) was cleaved from the fcc crystal structure with Pd–Pd lattice spacing 2.80 Å [30,31]. As shown in Fig. 2, there are three distinct adsorption sites including atop (CN=1), bridge (CN=2), and hollow (CN=3) [32], referring to adsorption of a hydrogen atom to one, two, and three metal atoms, respectively. In addition, the adsorption energies of H (E_{ad}) vary with hydrogen coordination. Among these adsorption sites, the 3-fold hollow sites are most energetically favorable, and the 1-fold atop sites are least favorable.

With respect to the palladium hydride, both clusters and surface (Figs. 1, S2, and S3) were constructed with H located in Pd octahedral site, which was reportedly the most suitable site [33]. When H atoms are placed in the subsurface sites of Pd_4 and Pd_{13}, they diffuse outside and form surface absorbed H spontaneously (Fig. S3). It is found that the presence of surface absorbed H is beneficial for the stability of

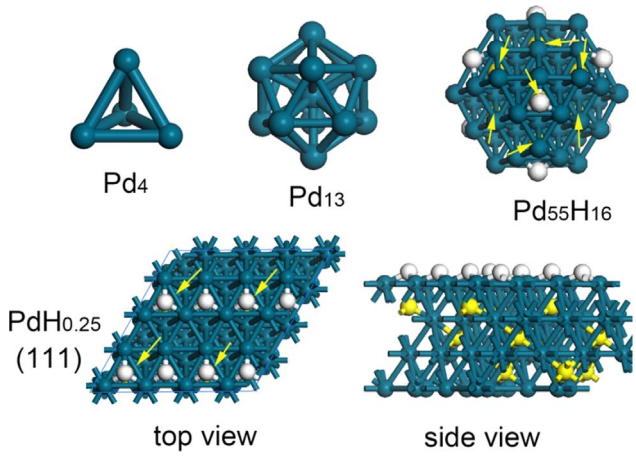

Fig. 1. Structures of Pd_4, Pd_{13}, $Pd_{55}H_{16}$ clusters (up); top view and side view of $PdH_{0.25}$ (111)-(4×4) surface. Pd, surface H atoms and bulk H atoms are in dark-blue, white and yellow (yellow arrow), respectively.

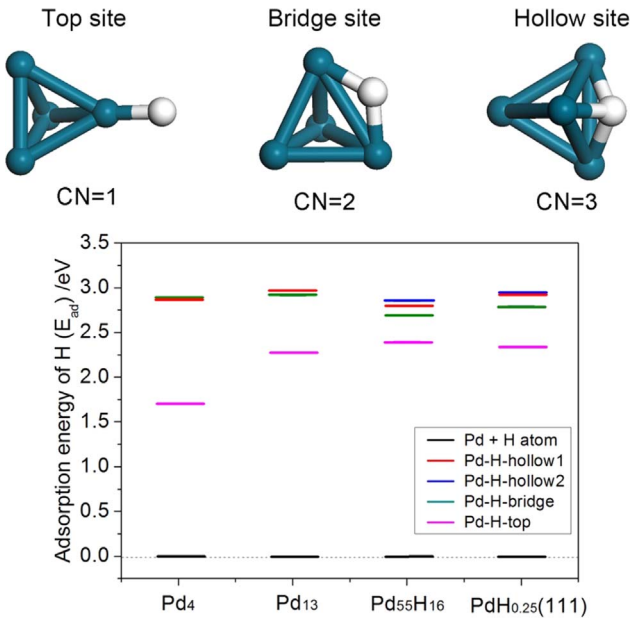

Fig. 2. Three distinct adsorption sites: atop, bridge and hollow site; and the adsorption energies of the H atom on various sites as function of Pd NPs size.

subsurface H. However, the subsurface H atoms would be stable only when all the surface sites are covered by H atoms, as previously reported by Zhou et al. [34]. In this case, the H/Pd ratio of configuration would reach up to 2.0, which is too high and not correspond to the real condition in the current study. With the increase of the size, palladium hydride can be stabilized at low coverage of surface absorbed H atoms. After optimization, $Pd_{55}H_{16}$ cluster was obtained. In the case of PdH_x(111) surface, it can be found that $PdH_{0.25}$ formed when only one H atom located inside Pd unit cell, which is coincident with the experiment results in the nano-Pd system [35].

Taking all the above structure optimization results into account, we chose pure Pd_4, Pd_{13}, $Pd_{55}H_{16}$ clusters, and $PdH_{0.25}$ (111) surface as the reasonable models for further calculations.

Consequently, the possible elementary steps of hydrogen evolution on the surface of Pd_4, Pd_{13}, $Pd_{55}H_{16}$, and $PdH_{0.25}$(111) were investigated using thermochemical analysis and DFT calculations [12]. Starting from the initial states (Hh) with H^* atoms adsorbed at the most stable 3-fold hollow sites [36], we calculated the possible pathways for hydrogen evolution from the two H^* to H_2^* followed by desorption of H_2^* from the Pd surface into a vacuum. The energy diagrams and optimized configurations of the intermediates and transition states are displayed in Figs. 3 and S4–11. For each of the four cases in Fig. 3, the formation of H_2 molecule from H^* consists of three steps (H^* diffusion, H^* combination, and H_2^* desorption), and all steps are endothermic. First, the adsorbed H^* atoms diffuse from the hollow sites to the bridge sites via a low barrier TS1, resulting in Hb state. Relative to Hh state, the energy barriers for H^* diffusions are 0.16, 0.13, 0.38 and 0.14 eV for Pd_4, Pd_{13}, $Pd_{55}H_{16}$ and $PdH_{0.25}$ (111), respectively. After the H^* combination step via TS2, the distance of H^*-H^* is further shortened with the two H^* atoms bound to the same Pd atom (Ht). The short H^*-H^* distances in the Ht state, being 0.845, 0.866, 0.845 and 0.861 Å for Pd_4, Pd_{13}, $Pd_{55}H_{16}$ and $PdH_{0.25}$(111) systems, respectively, which is comparable with the H-H bond lengths of activated H_2 and is slightly (~0.1 Å) longer than gas phase H_2 (0.747 Å) [28,37]. The formation of dihydrogen H_2^* needs to overcome energy barriers of 0.85, 0.67, 0.39 and 0.74 eV for Pd_4, Pd_{13}, $Pd_{55}H_{16}$ and $PdH_{0.25}$ (111) systems, respectively. In order to better show the processes for H^* diffusion and H^* combination, all the configurations and relative energies along the reaction path were also detailed in Figs. S12–S13. For the third step (H_2^* desorption), we also attempted to

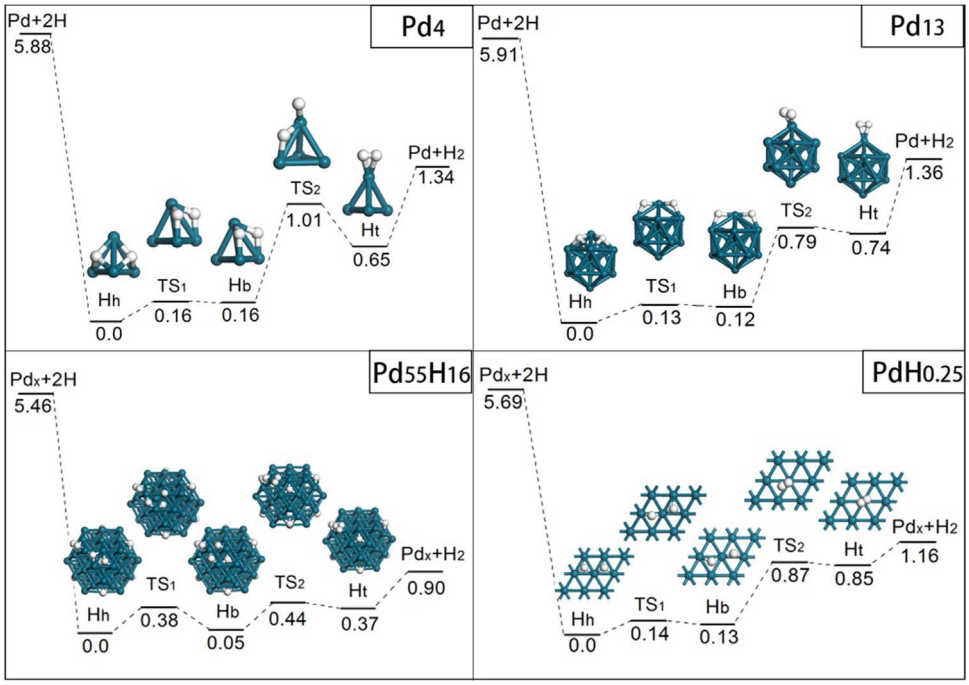

Fig. 3. Optimized configurations and calculated relative energy diagram in hydrogen evolution processes on Pd_4, Pd_{13}, $Pd_{55}H_{16}$ clusters and $PdH_{0.25}$ (111)-(4×4) surface.

locate a transition state for the step using CI-NEB method. However, no transition state could be located. Indeed, we observed that the energies rise monotonically with the distance between H_2 and Pd clusters increasing (Fig. S15).

It is an important elementary step for H_2 evolution that the diffusions of H atoms transport from the subsurface to the surface. We thus gave more attention. Calculations about subsurface H atoms were carried out. For the PdHx species with subsurface and surface H atoms simultaneously, surface H atoms react preferentially with each other and then combinative desorption from the surface in the form of H_2 molecule. Furthermore, the calculation results show that once disappearance of surface H adatoms after desorption of hydrogen, subsurface H atoms diffuse outside without barrier and form surface adsorbed H atoms (Fig. S14). Therefore, the step of bulk diffusion is negligible for overall H_2 evolution.

By comparing the energy barriers of each steps (summarized in Fig. 4), we determined that the step of H^* diffusion is much easier than the other two steps. The diffusion starting from a hollow site to a bridge site only need an energy of < 0.2 eV/atom, which is agree well with the experimental results of STM [38,39]. The combination of $2H^*$ on atop sites of $Pd_{55}H_{16}$ cluster involves a low energy barrier of 0.38 eV, while on the Pd_4, Pd_{13} and $PdH_{0.25}$ (111) surface, the energy barrier are as high as 0.85, 0.67 and 0.74 eV, respectively. With respect to the desorption of molecular H_2, the energy for sub-nano Pd_4 clusters is as high as 0.69 eV. As the cluster size increases, the energy decrease to 0.67 and 0.53 eV for Pd_{13} and $Pd_{55}H_{16}$, respectively, which is consistent with previously reported results [28]. The desorption energy of H_2 from the $PdH_{0.25}$ (111) surface is the smallest, and only 0.31 eV was required to overcome the barrier. These results suggest that the combination of $2H^*$ on medium-sized Pd cluster (Pd_{55}) is facile, and the H_2 evolution determined by the process of H_2 desorption with a energy barrier of 0.53 eV. While both the combination of $2H^*$ and H_2 desorption are very difficult for the sub-nanometer clusters, and the rate-limited step for large Pd NPs is the combination of $2H^*$ [34,40,41].

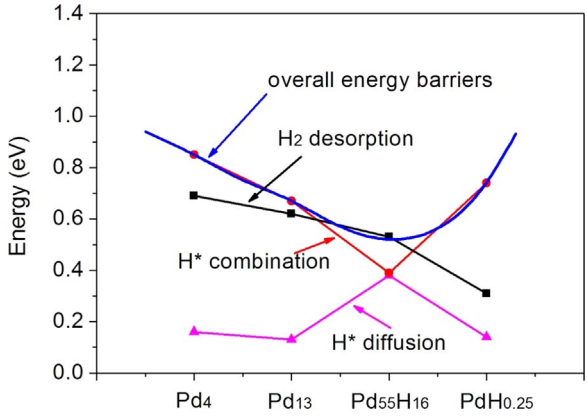

Fig. 4. Energy barriers of H^* diffusion on a Pd cluster surface (pink), H^* combination (red) and desorption of H_2 from Pd metal surface (blank), as well as the overall energy barriers of hydrogen evolution (blue).

For a certain reaction, the overall energy barrier should be the largest of the barriers for H evolution, which are depicted in Fig. 4 with blue line. Clearly, DFT calculations reveal that the Tafel reaction over Pd catalysts may be optimized by tuning the size of Pd NPs, because of the rate-limiting step of H_2 evolution for small clusters involves H^* combination and desorption of H_2, and that is the combination of $2H^*$ over large NPs. The overall barrier for the hydrogen evolution process decreased as the Pd size increased from Pd_4 (0.85 eV) to Pd_{55} (0.53 eV) then increase to 0.74 eV for large nanoparticles. Hence, the overall energy curve would be important for predicting the activities of supported-Pd catalysts.

Combining all the above DFT calculation results, it can be found that the reaction of favorable pathways is predominant occurred on the edge and corner sites of Pd NPs in the Pd cluster systems. And it is very difficult for H_2 formation on Pd terrace sites result from the strong adsorption of H atom. Moreover, once H_2 molecule attached to Pd surface, the hydrogen dissociation would happen spontaneously during the relaxation process (Fig. S13), which agree well with previous study [37]. But Pd (111) surface only provide well-defined terrace sites, which generally is considered as a less active site than others for many reactions [42,43]. Although for the appearance of new sites (top sites of 9-fold coordinated Pd atom) as the nanoparticle size increases, H_2 molecules could adsorption on Pd (111) surfaces. H_2 desorption is extremely easy to occur with the smallest desorption energy of 0.31 eV.Besides, compared with pure Pd cluster, there are slightly

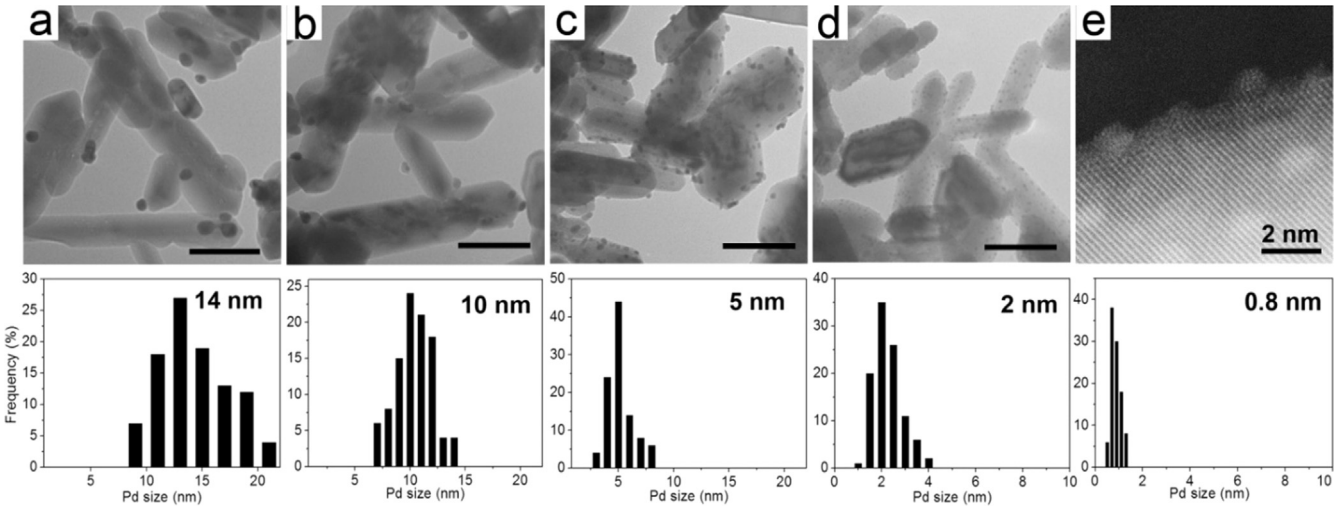

Fig. 5. (a–d) TEM images and the corresponding histograms of the particle-size distributions of the Pd/TiO_2 catalysts: a) 14 nm-Pd, b) 10 nm-Pd, c) 5 nm-Pd and d) 2 nm-Pd. The scale bar in the TEM images represents 100 nm. e) C_s-HAADF-STEM image and histogram of particle-size distributions for the 0.8 nm-Pd catalyst.

differences in pathways and relative energies of H_2 evolution on the surface of PdH_x. But it can be found that the steps of H_2 desorption and $2H^*$ combination for Pd_{55} and Pd (111) still are the rate-limiting steps with the energy barriers of 0.53 and 0.74 eV, suggesting that the effects of subsurface H atoms is negligible.

Based on mentioned above, a unique size dependence for H_2 evolution over Pd NPs can be predicted, that the $Pd_{55}H_{16}$ cluster (a diameter of 1.6 nm) with the lowest barrier (i.e. 0.53 eV) would exhibit the highest activity and the formation of Pd-H species would be benefit to H_2 evolution.

Hence, a series of TiO_2 nanorod-supported Pd catalysts (Pd/TiO_2) were prepared with a wide range of Pd NP sizes by the colloidal deposition method, which is an effective way to control the diameters of Pd nanoparticles and prepare uniform catalysts with small size [44]. TEM images of the Pd/TiO_2 catalysts and the corresponding histograms of the size distribution are shown in Fig. 5. Because the ultrafine Pd clusters cannot be well observed using traditional TEM and HRTEM (Fig. S17), C_s-HAADF-STEM was employed to detect Pd sub-nano clusters in the samples (Figs. 5e and S17). Obviously, TiO_2 exhibited a uniform rod-like morphology and Pd NPs with narrow size distribution were homogeneously dispersed on the surfaces of TiO_2 supports for each sample. The sizes of the Pd NPs in the various catalysts differed significantly from each other. In addition, the HRTEM (Fig. S18) studies revealed that the predominantly exposed planes are {111} in the large Pd NPs with a lattice spacing of 0.23 nm, especially when the size is more than 10 nm, which agree well with XRD results (Fig. S19). Therefore, Pd (111) can be chosen as a representative model of Pd NPs that are more than 10 nm in size. Based on these characterizations and analysis, TiO_2-supported Pd NPs with five different sizes were successfully obtained from sub-nanometer (0.8 nm) to 14 nm, which were denoted as 0.8 nm-Pd, 2 nm-Pd, 5 nm-Pd, 10 nm-Pd and 14 nm-Pd, according to the different the average size of Pd NPs in each sample.

The X-ray diffraction (XRD) patterns of the Pd/TiO_2 catalysts were measured and are shown in Fig. S19. For the various catalysts, peaks corresponding to the rutile-type TiO_2 phase (JCPDS 88-1173) and Pd-related reflection peaks were observed [45], except for the 0.8 nm-Pd and 2 nm-Pd samples. The absence of Pd reflection peaks resulted from the size of the Pd NPs being too small. The electronic properties of the Pd were also characterized by XPS because the different electronic structures may exert an effect on the H_2 evolution performance. The XPS spectra (Fig. S20) indicate that all of the samples exhibited two characteristic peaks (i.e., metallic Pd $3d_{5/2}$ and Pd $3d_{3/2}$) [46,47]. Note that 14 nm-Pd exhibits a Pd $3d_{5/2}$ peak at ~334.0 eV, while smaller Pd NPs exhibit much higher Pd $3d_{5/2}$ binding energy range from 334.2eV to 334.7 eV, revealing that stronger interaction between TiO_2 and Pd clusters occurred with the decrease of Pd NPs size [48].

As a hydrogen reservoir and active medium, β-PdH_x specie is more stable than α-PdH_x (H/Pd=0.03)[49,50] and plays a key role in hydrogen- related reactions [51–53]. In addition, the kinetics of the PdH_x decomposition process [54], which involves bulk diffusion, transport from the bulk to the subsurface and surface and recombination desorption of hydrogen from the surface [55], is controlled by desorption of the chemisorbed state H [56,57], because the activation energy is considerably larger than that for bulk diffusion [58]. Therefore, temperature-programmed hydride decomposition (TPHD) under hydrogen atmosphere, an effective technique for investigating the H-Pd binding strength as well as the behavior of hydrogen desorption [34], were carried out to check the size effect of palladium on the efficiency of hydrogen evolution.

Fig. 6 shows the TPHD profiles for all of the Pd/TiO_2 catalysts. Except for pure TiO_2, remarkably sharp negative peaks appear below 100 °C for all of the samples, which can be assigned to hydrogen evolution from the decomposition of β-PdH_x [59,60]. The intensity of the peaks increased linearly as the size of Pd NPs increased due to the formation of more β-PdH_x in larger Pd NPs [34,61]. The H/Pd ratio (Table 1) is an effective descriptor for representing hydrogen solubility [62]. In the current study, a slight increase in the H/Pd ratio from 0.14 to 0.25 as the function of the Pd NP size was observed, indicating that the chemisorbed state H (Pd-H phase) primarily settles down on the surface and subsurface (H/Pd=0.6 for a crystalline PdH) [34,63].

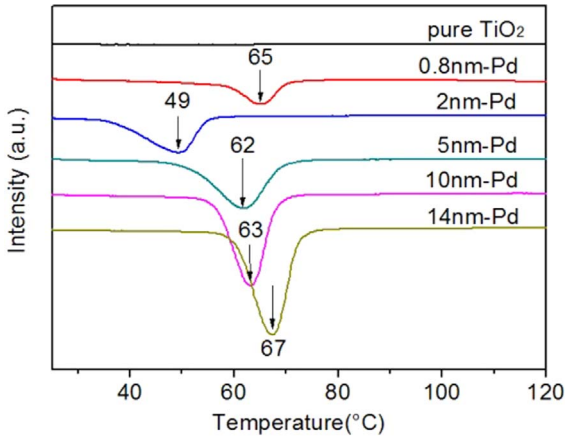

Fig. 6. Temperature-programmed hydride decomposition (TPHD) profiles of five Pd/TiO_2 catalysts and pure TiO_2.

Table 1
Pd loading [Pd], amount of hydrogen desorption (A_H) and the H/Pd ratios.

Sample	[Pd] wt%	A_H mmol H_2/gPd	H/Pd ratio
0.8 nm-Pd	0.33	1.30	0.14
2 nm-Pd	1.79	1.65	0.17
5 nm-Pd	1.81	1.63	0.17
10 nm-Pd	1.82	2.00	0.21
14 nm-Pd	1.80	2.34	0.25

Furthermore, the Pd/H ratio are similar with DFT calculations, suggesting the rationality of PdH_x structures. Most importantly, significant differences in the TPHD peak positions were observed, indicating that the Pd NP size has an effect on the stability of the Pd-H species [64]. A peak corresponding to H_2 evolution was observed at approximately 65 °C for the 0.8 nm-Pd sample. Then, as the size of the Pd NPs increased, the peak of the 2 nm-Pd catalyst shifted to 49 °C, indicating a significant increase in the activity of H_2 evolution. Interestingly, however, a considerable increase in the desorption temperature (62 °C) for the 5 nm-Pd catalyst was observed, and the temperature of H_2 evolution was even higher for the 10 nm-Pd catalysts, where the peak was centered 63 °C. The 14 nm-Pd catalyst exhibited the highest temperature for the H_2 desorption peak (i.e., 67 °C). Although 10 nm-Pd and 14 nm-Pd were both big enough to be represented by $PdH_{0.25}$(111), a obvious different in TPHD profiles was observed. In fact, the series of supported Pd/TiO_2 catalysts consist of an assembly of Pd NPs with a certain size distribution. For catalyst of 14 nm-Pd, TEM images show that the size of Pd NPs concentrated in the range of 10–20 nm and it is rarely found the Pd NPs less than 10 nm. In the sample of 10 nm-Pd, however, a portion of Pd NPs are less than 10 nm in size. Therefore, the low-temperature region of peak of 10 nm-Pd shows an obvious different with 14 nm-Pd. These results further confirm that H_2 evolution is difficult over sub-nano Pd clusters and larger NPs, while the formation and desorption of H_2 is favored from moderately sized Pd NPs (2 nm-Pd), which is consistent with the results of DFT calculations.

As a promising hydrogen-storage medium, formate can afford ultraclean H_2 with free of CO via catalytic dehydrogenation according to the following reaction [65–67]:

$$HCOO^- + H_2O = HCO_3^- + H_2 \quad (1)$$

Supported-Pd catalysts are typically considered to be best suitable for this reaction [68–70]. However, previous studies showed that dehydrogenation of formate over Pd NPs proceeded well only at elevated temperatures and was completely inactive under ambient conditions due to the difficulty of the combinative desorption of hydrogen [13–15].

The catalytic activities for the dehydrogenation of formate over the five Pd/TiO_2 catalysts with different Pd sizes were investigated in neat water at room temperature. The data (Fig. S21), hydrogen generations from different formate salts dehydrogenation, indicate that ammonium formate is a suitable hydrogen-storage material with the highest activity in the presence of 2 nm-Pd catalyst. Gas chromatography (GC, Figs. S22–23) and Fourier transform infrared spectroscopy (FTIR, Fig. S24) were performed to analyze the composition of the gas products. Only hydrogen and trace amounts of CO_2, which resulted from the decomposition of HCO_3^- [69], were detected. Note that while CO is the typical by-products of the reaction in formic acid/formate system [13,65], no detectable gaseous CO signal was observed. These results indicate that high-purity hydrogen can be generated from the dehydrogenation of formate.

The catalytic performances for ammonium formate dehydrogenation over all of the catalysts are shown in Fig. 7a. The amount of hydrogen produced increased with time for all of the samples, except the 14 nm-Pd sample. The 2 nm-Pd catalyst exhibited the best H_2 production efficiency followed by the 0.8 nm-Pd and 5 nm-Pd catalysts. When the size of the Pd NPs is up to 10 nm, the volume of H_2 generation is negligible. The initial turnover frequency (TOF) values were also measured within the first 10 min with the assumption that only surface Pd atoms were accessible, where the dispersions of metal atoms were calculated from the CO chemisorptions. Notably, Fig. 7b shows that the TOF values for the dehydrogenation of $HCOONH_4$ (2184 h^{-1}) and HCOONa (1673 h^{-1}, Fig. S21) over the 2 nm-Pd sample were higher than those for previously reported catalysts at room temperature (Table S1), even comparable to those at elevated temperatures. In addition, a volcano relationship between the TOF values and the Pd NP size was observed. As the size of the Pd NPs increased from sub-nano (0.8 nm-Pd) to nanometer (2 nm-Pd) sized, TOF value increased sharply from 297 h^{-1} to 2184 h^{-1} and then decreased substantially with a further increase in the Pd size even to zero for sample of the 14 nm-Pd.

Fig. 7c shows the hydrogen generation rate for 2 nm-Pd catalyzed $HCOONH_4$ dehydrogenation at different temperatures. To determine the apparent activation energy (E_a), Arrhenius analyses of the initial rate (Fig. 7d) were performed within a temperature range of 20–70 °C. The 2 nm-Pd catalyst exhibited the lowest E_a (37.0 ± 2 kJ mol^{-1}), which was even lower than that of a previously reported homogeneous catalyst (41 kJ mol^{-1}) [66]. Although the E_a of 0.8 nm-Pd (46.5 ± 3 kJ mol^{-1}) was larger than that of 2 nm-Pd, it was still similar to the value in the literature. However, for the 5 nm-Pd catalyst with a larger Pd NP size, the E_a increase substantially to 59.2 ± 1 kJ mol^{-1}, and the E_a is indeed up to 64.2 ± 3 kJ mol^{-1} and 75.1 ± 6 kJ $mol^{-1}$for the 10 nm-Pd and 14 nm-Pd catalysts. Based on DFT calculations, the activation energies were 64.5 kJ mol^{-1}, 51.0 kJ mol^{-1} and 71.3 kJ mol^{-1} in Tafel reaction catalyzed by Pd_{13}, $Pd_{55}H_{16}$ and $PdH_{0.25}$ (111), which were chosen as representatives for the samples of 0.8 nm-Pd, 2 nm-Pd and >10 nm-Pd catalysts, respectively. Obviously, the E_a catalyzed by the three kinds of Pd catalysts were basically consistent with and slightly smaller than the $E_a$calculated with theoretical studies. The difference of apparent activation energy most likely attribute to the potential impact of Pd-TiO_2interaction [15]. As mentioned above, the XPS spectra show that the smaller Pd NPs exhibit the stronger interaction between TiO_2 and Pd clusters. However the relationship between the catalytic activities and the Pd NP size exhibits a volcano shape. These results suggest that the size effect should be the primary factor to affect the activity of H_2 evolution and formate dehydrogenation in Pd/TiO_2 systems.

As an important characteristic of catalysts, the durability also has been tested and the results were shown in Fig. S25. A slight deactivation can be observed over the 2nd run, because the size of Pd NPs became larger (the average diameter of Pd NPs increased from 2.1nm to 3.2 nm) after the 3rd catalytic dehydrogenation reaction of formate (Fig. S26). This result further illustrate that the size of Pd NPs is a key factor for catalytic Tafel reaction. Nevertheless, it will be necessary to improve the durability of the Pd catalysts for practical applications [69,71].

Overall, a prominent size-dependent activity for the dehydrogenation of formate over Pd NPs that ranged in size from 0.8 to 14 nm was observed, and ~2 nm Pd NPs was the optimum catalyst. The volcano-like curve for the TOF values for H_2 evolution is consistent with the DFT and TPHD results, elucidating H_2 evolution plays a key role in the dehydrogenation of formate in the Pd-based catalyst system.

4. Conclusion

In summary, we have demonstrated that H_2 evolution over Pd nanocatalysts was governed by two reaction steps of Tafel reaction: H^* combination was very difficult over the large Pd NPs, while the rate-limiting step for media-sized Pd cluster is H_2 desorption. Moreover, both H^* combination and desorption of molecular H_2 are sluggish on the sub-nanometer Pd clusters. Pd NPs with a diameter of 2 nm

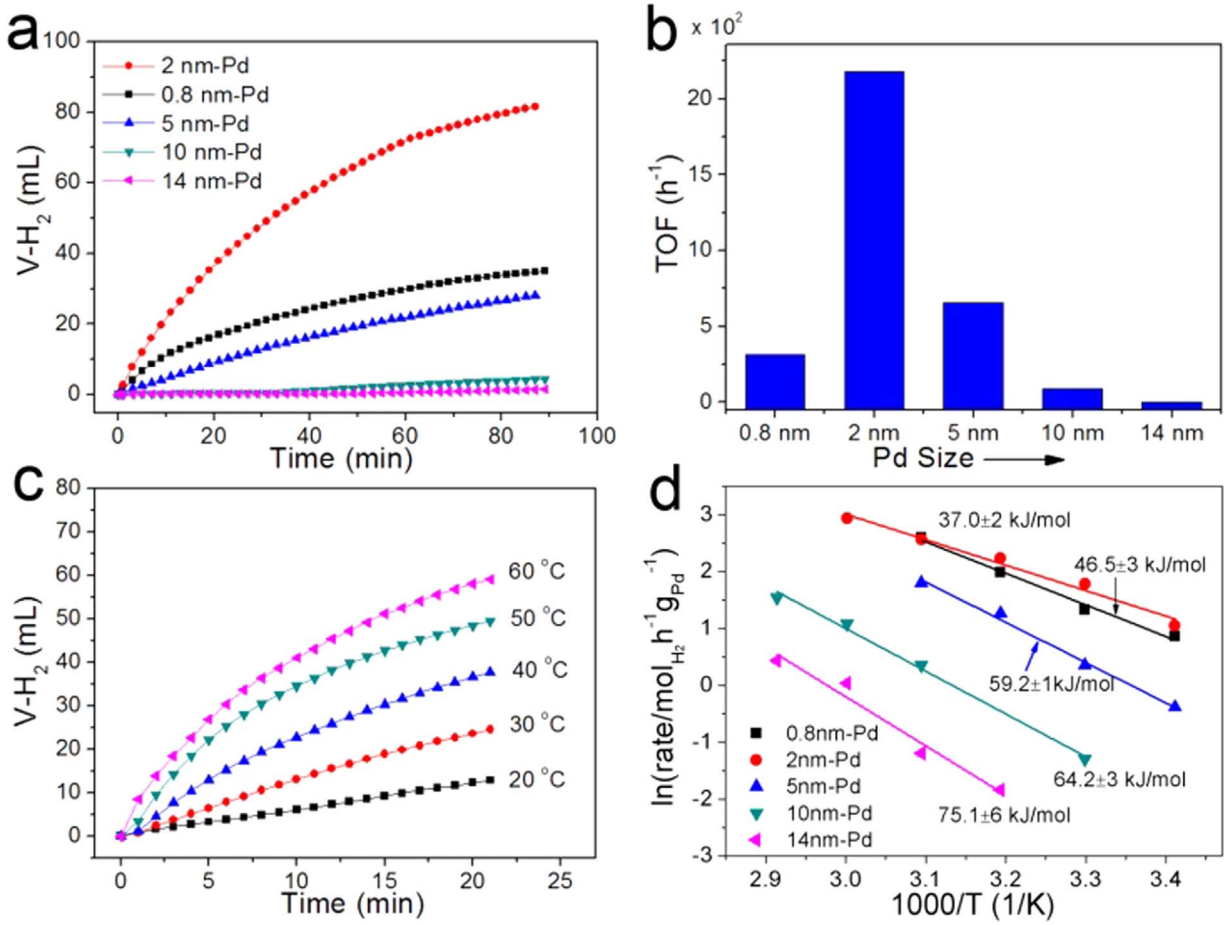

Fig. 7. a) H_2 evolution via dehydrogenation of aqueous ammonium formate (2 M, 10 mL) at room temperature (298 K) as a function of time. b) Size dependence of initial TOF for the Pd/TiO_2 catalysts. The TOF was measured within the first 10 min c) Kinetic traces for H_2 evolution as a function of time catalyzed by 2 nm-Pd at different temperatures (20–60 °C). Reaction conditions: 10 mL scale of 2 M aqueous $HCOONH_4$, 5.0 μmol Pd. d) Arrhenius plots of the reaction rates for the Pd/TiO_2 catalysts.

exhibited excellent catalytic activity for hydrogen evolution both for temperature-programmed palladium hydride decomposition and catalytic dehydrogenation of formate. This found mental insight will be benificial for the design of novel high-performance catalysts for efficient H_2 evolution with important implications for the development of the hydrogen economy.

Acknowledgements

This work was supported by the National Natural Science Foundation of China (21473199), Beijing Municipal Science & Technology Commission and Chinese Academy of Sciences. DFT calculations were supported by the Beijing Computing Center. We thank prof. Zhixiang Wang for helpful discussion.

Appendix A. Supplementary material

Supplementary data associated with this article can be found in the online version at doi:10.1016/j.nanoen.2017.02.001.

References

[1] M. Grasemann, G. Laurenczy, Energy Environ. Sci. 5 (2012) 8171–8181.
[2] K. Christopher, R. Dimitrios, Energy Environ. Sci. 5 (2012) 6640–6651.
[3] Q.-L. Zhu, Q. Xu, Energy Environ. Sci. 8 (2015) 478–512.
[4] D. Barreca, G. Carraro, V. Gombac, A. Gasparotto, C. Maccato, P. Fornasiero, E. Tondello, Adv. Funct. Mater. 21 (2011) 2611–2623.
[5] Q.P. Wu, F. Huang, M.S. Zhao, J. Xu, J.C. Zhou, Y.S. Wang, Nano Energy 24 (2016) 63–71.
[6] W. Sheng, M. Myint, J.G. Chen, Y. Yan, Energy Environ. Sci. 6 (2013) 1509–1512.
[7] X. Chia, A. Adriano, P. Lazar, Z. Sofer, J. Luxa, M. Pumera, Adv. Funct. Mater. 26 (2016) 4306–4318.
[8] L. Zhang, Q. Chang, H. Chen, M. Shao, Nano Energy (2016). http://dx.doi.org/10.1016/j.nanoen.2016.1002.1044i.
[9] Y. Li, H. Wang, L. Xie, Y. Liang, G. Hong, H. Dai, J. Am. Chem. Soc. 133 (2011) 7296–7299.
[10] B. Hinnemann, P.G. Moses, J. Bonde, K.P. Jørgensen, J.H. Nielsen, S. Horch, I. Chorkendorff, J.K. Nørskov, J. Am. Chem. Soc. 127 (2005) 5308–5309.
[11] Y. Yamada, T. Miyahigashi, H. Kotani, K. Ohkubo, S. Fukuzumi, J. Am. Chem. Soc. 133 (2011) 16136–16145.
[12] J.A. Herron, J. Scaranto, P. Ferrin, S. Li, M. Mavrikakis, ACS Catal. 4 (2014) 4434–4445.
[13] K. Jiang, K. Xu, S. Zou, W.B. Cai, J. Am. Chem. Soc. 136 (2014) 4861–4864.
[14] Q.-L. Zhu, N. Tsumori, Q. Xu, Chem. Sci. 5 (2014) 195–199.
[15] Q.Y. Bi, J.D. Lin, Y.M. Liu, X.L. Du, J.Q. Wang, H.Y. He, Y. Cao, Angew. Chem. Int. Ed. 53 (2014) 13583–13587.
[16] W. Sheng, Z. Zhuang, M. Gao, J. Zheng, J.G. Chen, Y. Yan, Nat. Commun. 6 (2015) 5848.
[17] J.R. Kitchin, J.K. Norskov, M.A. Barteau, J.G. Chen, Phys. Rev. Lett. 93 (2004) 156801.
[18] J.K. Nørskov, T. Bligaard, A. Logadottir, J.R. Kitchin, J.G. Chen, S. Pandelov, U. Stimming, J. Electrochem. Soc. 152 (2005) J23–J26.
[19] S. Harinipriya, M.V. Sangaranarayanan, Langmuir 18 (2002) 5572–5578.
[20] S. Bai, C. Wang, M. Deng, M. Gong, Y. Bai, J. Jiang, Y. Xiong, Angew. Chem. Int. Ed. 53 (2014) 12120–12124.
[21] J. Greeley, J.K. Norskov, L.A. Kibler, A.M. El-Aziz, D.M. Kolb, ChemPhysChem 7 (2006) 1032–1035.
[22] T.A. Maark, A.A. Peterson, J. Phys. Chem. C 118 (2014) 4275–4281.
[23] M.K. Oudenhuijzen, J.A.V. Bokhoven, J.T. Miller, D.E. Ramaker, D.C. Koningsberger, J. Am. Chem. Soc. 127 (2005) 1530–1540.
[24] C. Hu, S.-W. Ting, K.-Y. Chan, W. Huang, Int. J. Hydrogen Energy 37 (2012) 15956–15965.
[25] S.H. Mushrif, A.D. Rey, G.H. Peslherbe, J. Mater. Chem. 20 (2010) 10503–10510.
[26] E. Cui, G. Lu, J. Phys. Chem. C 117 (2013) 26415–26425.
[27] D.E. Nanu, A.J. Böttger, Adv. Funct. Mater. 18 (2008) 898–906.
[28] X. Liu, D. Tian, C. Meng, J. Mol. Struct. 1080 (2015) 105–110.
[29] I.V. Yudanov, A. Genest, S. Schauermann, H.J. Freund, N. Rosch, Nano Lett. 12

(2012) 2134–2139.
[30] R. Zhang, H. Liu, B. Wang, L. Ling, J. Phys. Chem. C 116 (2012) 22266–22280.
[31] M. Mahapatra, W.T. Tysoe, J. Phys. Chem. C 120 (2016) 2309–2319.
[32] W. Dong, J. Hafner, Phys. Rev. B 93 (1997) 15396–15403.
[33] S. Hong, T.S. Rahman, Phys. Rev. B 75 (2007) 155405.
[34] C. Zhou, S. Yao, J. Wu, R.C. Forrey, L. Chen, A. Tachibana, H. Cheng, Phys. Chem. Chem. Phys. 10 (2008) 5445–5451.
[35] M. Bonarowska, J. Pielaszek, W. Juszczyk, Z. Karpiński, J. Catal. 195 (2000) 304–315.
[36] G.W. Watson, R.P.K. Wells, D.J. Willock, G.J. Hutchings, J. Phys. Chem. B 105 (2001) 4889–4894.
[37] Y. Zhao, D. Tian, Comput. Theor. Chem. 991 (2012) 40–43.
[38] T. Mitsui, M.K. Rose, E. Fomin, D.F. Ogletree, M. Salmeron, Nature 422 (2003) 705–707.
[39] T. Mitsui, M.K. Rose, E. Fomin, D.F. Ogletree, M. Salmeron, Surf. Sci. 540 (2003) 5–11.
[40] C. Zhou, S. Yao, J. Wu, L. Chen, R.R. Forrey, H. Cheng, J. Comput. Theor. Nanosci. 6 (2009) 1320–1327.
[41] F.R. Lucci, M.T. Darby, M.F. Mattera, C.J. Ivimey, A.J. Therrien, A. Michaelides, M. Stamatakis, E.C. Sykes, J. Phys. Chem. Lett. 7 (2016) 480–485.
[42] D. Gao, H. Zhou, J. Wang, S. Miao, F. Yang, G. Wang, J. Wang, X. Bao, J. Am. Chem. Soc. 137 (2015) 4288–4291.
[43] W. Zhu, R. Michalsky, O. Metin, H. Lv, S. Guo, C.J. Wright, X. Sun, A.A. Peterson, S. Sun, J. Am. Chem. Soc. 135 (2013) 16833–16836.
[44] Y. Önal, J. Catal. 223 (2004) 122–133.
[45] Z. Zhu, H. Tan, J. Wang, S. Yu, K. Zhou, Green Chem. 16 (2014) 2636–2643.
[46] V. Vaiano, G. Iervolino, G. Sarno, D. Sannino, L. Rizzo, J.J. Murcia Mesa, M.C. Hidalgo, J.A. Navío, Oil Gas Sci. Technol. – Rev. Inst. Fr. Pet. 70 (2015) 891–902.
[47] F. Yang, S.-C. Kung, M. Cheng, J.C. Hemminger, R.M. Penner, ACS Nano 4 (2010) 5233–5244.
[48] M. Hattori, H. Einag, T. Daio, M. Tsuji, J. Mater. Chem. A 3 (2015) 4453–4461.
[49] V. Bérubé, G. Radtke, M. Dresselhaus, G. Chen, Int. J. Energy Res. 31 (2007) 637–663.
[50] A. Chen, C. Ostrom, Chem. Rev. 115 (2015) 11999–12044.
[51] A. Valcarcel, F. Morfin, L. Piccolo, J. Catal. 263 (2009) 315–320.
[52] S.K. Kim, C. Kim, J.H. Lee, J. Kim, H. Lee, S.H. Moon, J. Catal. 306 (2013) 146–154.
[53] R. Griessen, N. Strohfeldt, H. Giessen, Nat. Mater. Lett. 15 (2016) 311–317.
[54] W.D. Michalak, J.B. Miller, D.R. Alfonso, A.J. Gellman, Surf. Sci. 606 (2012) 146–155.
[55] W. Xie, D.J. West, Y. Sun, S. Zhang, Nano Energy 2 (2013) 742–748.
[56] S. Ohno, M. Wilde, K. Fukutani, J. Chem. Phys. 140 (2014) 134705.
[57] S. Schauermann, H.J. Freund, Acc. Chem. Res. 48 (2015) 2775–2782.
[58] R.J. Behm, J. Chem. Phys. 78 (1983) 7486–7490.
[59] A.-G. Boudjahem, A. Redjel, T. Mokrane, J. Ind. Eng. Chem. 18 (2012) 303–308.
[60] A. Drelinkiewicz, A. Waksmundzkagora, W. Makowski, J. Stejskal, Catal. Commun. 6 (2005) 347–356.
[61] K. Möbus, E. Grünewald, S.D. Wieland, S.F. Parker, P.W. Albers, J. Catal. 311 (2014) 153–160.
[62] S. Syrenova, C. Wadell, F.A. Nugroho, T.A. Gschneidtner, Y.A. Diaz Fernandez, G. Nalin, D. Switlik, F. Westerlund, T.J. Antosiewicz, V.P. Zhdanov, K. Moth-Poulsen, C. Langhammer, Nat. Mater. Lett. 14 (2015) 1236–1244.
[63] N.K. Nag, J. Phys. Chem. B 105 (2001) 5945–5949.
[64] Y.S. Au, M.K. Obbink, S. Srinivasan, P.C.M.M. Magusin, K.P. de Jong, P.E. de Jongh, Adv. Funct. Mater. 24 (2014) 3604–3611.
[65] A. Boddien, F. Gartner, C. Federsel, P. Sponholz, D. Mellmann, R. Jackstell, H. Junge, M. Beller, Angew. Chem. Int. Ed. 50 (2011) 6411–6414.
[66] G. Papp, J. Csorba, G. Laurenczy, F. Joo, Angew. Chem. Int. Ed. 50 (2011) 10433–10435.
[67] Katerina Sordakis, A.F. Dalebrook, G. Laurenczy, ChemCatChem 7 (2015) 2332–2339.
[68] K. Tedsree, T. Li, P.A.J. Bagot, S. Jones, E.A. Marquis, C.A. Chan, George D.W. Smith, K.M.K. Yu, S.C.E. Tsang, Nat. Nanotechnol. 6 (2011) 302–307.
[69] Z.L. Wang, J.M. Yan, H.L. Wang, Y. Ping, Q. Jiang, Sci. Rep. 2 (2012) 598.
[70] J. Su, L. Yang, M. Lu, H. Lin, ChemSusChem 8 (2015) 813–816.
[71] Q.L. Zhu, N. Tsumori, Q. Xu, J. Am. Chem. Soc. 137 (2015) 11743–11748.

Jin Wang was born in Shandong province and studied chemistry and material science at the University of Chinese Academy of Sciences in Beijing, where she completed her Ph.D. in 2016 in the group of Prof. Kebin Zhou. Her research focuses on the synthesis of nano- and subnano-metal catalysts for the application in environment and energy.

Hongyi Tan received his Ph.D. degree in Material Science in 2016 at the University of Chinese Academy of Sciences, under the supervision of Prof. Kebin Zhou. His research focuses on applications of nanomaterials with well-defined structures as heterogeneous catalysts.

Dan Jiang received her Master's degree in Materials from the School of Chemistry and Chemical Engineering, University of Chinese Academy of Sciences under the supervision of Prof. Kebin Zhou in 2016. Her current research interests focus on the synthesis of nanostructured catalytic materials and their application in environmental processes.

Kebin Zhou received his Ph.D. in Environmental Chemistry in 2003 at the Research Center for Eco-Environmental Sciences, Chinese Academy of Sciences, under the supervision of Prof. Xiaobai Xu. He carried out postdoctoral research in 2005 at Tsinghua University with Prof. Yadong Li. He is currently Professor of Chemistry at University of Chinese Academy of Sciences. His research focuses on novel nanostructured catalytic materials for environmental and energy applications.